ScienceAdvances
AAAS

Bayesian-Learning-Assisted Catalyst Discovery for Efficient Iridium Utilization in Electrochemical Water Splitting

Xiangfu Niu[1, †], Yanjun Chen[2,3, †], Mingze Sun[2], Satoshi Nagao[4], Yuki Aoki[4], Zhiqiang Niu[2], and Liang Zhang[1]*

[1]Center for Combustion Energy, School of Vehicle and Mobility, State Key Laboratory of Intelligent Green Vehicle and Mobility, Tsinghua University Beijing, 100084, China

[2]State Key Laboratory of Chemical Engineering, Department of Chemical Engineering, Tsinghua University, Beijing, China

[3]Department of Chemical Engineering, Sichuan University, Chengdu 610065, China

[4]Toyota Motor Corporation, Aichi-ken 471-8571, Japan

†These authors contributed equally: Xiangfu Niu, Yanjun Chen

*Corresponding author: Liang Zhang, email: zhangbright@tsinghua.edu.cn, orcid id: 0000-0002-9718-0436.

Abstract

Reducing noble metal dependence in oxygen evolution reaction (OER) catalysts is essential for achieving sustainable and scalable green hydrogen production. Bimetallic oxides, with their potential for high catalytic performance and reduced noble metal content, represent promising alternatives to traditional IrO_2-based OER catalysts. However, optimizing these materials remains challenging due to the complex interplay of elemental selection, composition, and chemical ordering. In this study, we integrate density functional theory (DFT) calculations with Bayesian learning to accelerate the discovery of high-performance, low-Ir bimetallic oxides, identifying surface Ir-doped TiO_2 as an optimal catalyst. Guided by theoretically optimized surface compositions and oxygen vacancies, we synthesized atomically dispersed Ir on TiO_2, achieving a 23-fold increase in Ir mass-specific activity and a 115 mV reduction in overpotential compared to commercial IrO_2. This work exemplifies a sustainable, data-driven pathway for electrocatalyst design that minimizes noble metal usage while maximizing efficiency, advancing scalable solutions in renewable energy and hydrogen production.

Introduction

Green hydrogen produced from renewable energy sources from is a promising energy carrier that can address global energy security, mitigate climate change, and reduce environmental pollution (*1, 2*). Electrochemical water splitting, particularly proton exchange membrane water electrolysis (PEMWE), offers high current density and rapid responsiveness, making it suitable for coupling with intermittent renewable energy sources such as wind and solar (*3*). A key bottleneck in water electrolysis is the oxygen evolution reaction (OER) at the anode, which involves complex multi-electron transfer steps and requires efficient and stable electrocatalysts. Currently, Ir-based oxides, particularly IrO_2, are the most effective catalysts for OER in acidic environments due to their optimal balance of activity and stability. Yet, the scarcity and high cost of iridium limit the scalability of these catalysts, posing a major challenge for the commercialization of PEMWE, making it crucial to reduce noble metal content for cost-effective hydrogen production.

Strategies such as catalyst support, doping, and defect engineering have been explored to reduce iridium usage (*4*). Loading active noble metal species onto a supporting substrate or incorporation of non-noble metals alongside iridium oxides offers effective ways to reduce the consumption of precious metals (*5*). Intriguingly, it's has also been discovered that the inert non-noble metal oxides, such as Ti and Ce, can be activated by noble element, enabling them to serve as active sites and participate in OER process (*6-8*). Additionally, their tunable structures enable further enhancements in catalytic performance and conductivity through chemical ordering and defect engineering (*9, 10*). These structural flexibility enables bimetallic oxides to reduce noble metal content while enhancing catalytic activity through synergistic effects between guest and host elements (*11*). However, despite these advantages, optimizing bimetallic oxides remains challenging due to the complex interplay between elemental composition, chemical ordering, and structural defects, which collectively influence catalytic activity and stability. Experimental trial-and-error and high-throughput computations alone are often insufficient for efficiently navigating the vast configuration space.

Bayesian optimization combined with machine learning surrogate model offers a powerful approach for efficiently identifying high-performance candidate materials from a vast configuration space (*12, 13*). In this study, we leverage an effective data-driven approach that combines density functional theory (DFT) with Bayesian optimization to efficiently explore and optimize bimetallic oxide catalysts for OER. By calculating the theoretical overpotential for each element in 66 different binary oxides, we identified Ir-doped TiO_2 as a highly promising combination due to its potential for dual active sites. Using a Gaussian process-based Bayesian optimization, we fine-tuned the Ir surface composition, chemical ordering and oxygen vacancies, finding that an Ir surface ratio of around 12.5% could achieve more than 40-fold increase in calculated Ir mass-specific activity compared to rutile IrO_2. This enhancement is attributed to the introduction of Ir and oxygen vacancies, which enhance Ti site activity while maintaining Ir site performance. Guided by these theoretical insights, we synthesized atomically dispersed Ir on TiO_2 with optimized oxygen vacancies, achieving a 23 times enhancement in Ir mass-specific activity and lowered the overpotential by 115 mV relative to commercial IrO_2. This work exemplifies a sustainable approach to catalyst discovery, reducing noble metal content and advancing the development of scalable, high-performance electrocatalysts for green hydrogen production.

Results and Discussion

Initial Screening

The search for binary oxide began with the identification of suitable alloying elements (Figure 1A). Considering rutile-type IrO_2 oxide as the state-of-the-art commercial OER electrocatalyst, the thermodynamically stable (110) surface model for rutile was utilized as the support substrate. Although some non-rutile-type oxides loaded with noble metals have achieved excellent activity, such as the work by Li et al. on Ir loaded onto γ-MnO_2 (*14*), we selected the classical rutile-type oxide support in this work to verify the effectiveness of Bayesian learning. The doping structures were constructed by replacing a host atom in coordinately unsaturated site (CUS) with a guest atom, as depicted in Figure S1. Six different rutile oxide supports (IrO_2, MoO_2, TiO_2, MnO_2, PdO_2, and SnO_2) were selected and doped with eleven potential guest elements (Au, Ir, Mn, Mo, Nb, Pt, Re, Ru, Sn, Ti, V). The selected oxide supports all adopt the rutile structure, including IrO_2 and five structurally compatible oxides (PdO_2, RuO_2, TiO_2, SnO_2, MoO_2) to ensure consistent comparison. Dopants were chosen based on their presence in the selected oxides (Ir, Pd, Ru, Ti, Sn, Mo) and extended to V, Re, Pt, Nb, Mn, and Au to cover a broader range of chemical properties. Systems with excessive structural distortion upon doping were excluded to ensure reliable screening results. To evaluate OER activity, the theoretical overpotential for doped atoms and their neighboring host atoms were calculated by computational hydrogen electrode method (*15, 16*).

Figure 1B illustrates OER activity of 66 kinds of binary oxides. As expected, Ir sites in IrO_2 exhibit outstanding activity. It is well known that RuO_2 exhibits higher OER activity than IrO_2, but its activity calculated by DFT is lower than IrO_2 in Figure 1B. This underestimation has also been widely reported in previous studies and is generally attributed to systematic errors inherent in DFT, or to the possibility that RuO_2 follows a different reaction pathway or involves alternative active sites (*17, 18*). For oxides such as RuO_2, PdO_2, MnO_2, and IrO_2, doping has a relatively minor effect on the activity of the host elements. In contrast, the activity of Sn and Ti sites in SnO_2 and TiO_2, respectively, is significantly influenced by the choice of doped elements. Notably, substantial enhancements in OER activity are observed at the Ti site when noble metals like Ir and Ru are doped into TiO_2. Considering both the activity of guest and host element sites, as well as the cost-effectiveness of the TiO_2 support, we selected Ir-doped TiO_2 as the optimal binary oxide combination. Previous work by Nørskov and co-workers has demonstrated the potential of Ir-doped TiO_2 as an effective OER catalyst (*19*). Moreover, several experimental studies have reported Ir-supported titanium oxides, lending further credibility to our screening approach (*20, 21*). Building on our screening results and the foundation laid by previous studies focused on compositional aspects, this work further deepens the understanding of IrTi mixed oxides by systematically tuning both the Ir content and the concentration of oxygen vacancies.

Figures 1C and 1D present the DFT-calculated OER free energy profiles for Ti and Ir sites in Ir-TiO_2 with respect to pure TiO_2. Pure TiO_2 shows poor OER activity due to its weak adsorption affinity for oxygenated intermediates. Upon doping with Ir, the adsorption strength at the Ti site significantly improves, reducing the free energy change for the potential-determining step (PDS) , i.e. the oxidation of OH* to O*, from 2.82 eV in pure TiO_2 to 1.76 eV in Ir-TiO_2. For the Ir site, the free energy change of the PDS in Ir-TiO_2 (1.67 eV) is comparable to that of IrO_2 (1.73 eV). Consequently, both Ti and Ir sites in $IrTiO_2$ demonstrate high OER activity, benefiting from the synergistic effects of Ir doping.

Bayesian Optimization of Surface Composition

Bayesian optimization was employed to identify the optimal surface composition and chemical ordering for Ir-TiO_2. A machine learning model capable of predicting activity across different Ir surface ratios and chemical arrangements was developed. Information about the environment of the adsorption site, such as atomic count, coordination numer, and other related features, was extracted as inputs for the machine learning model (Figure S2, Figure S3). The difference in adsorption free energies between oxygen and hydroxyl, ΔG_O - ΔG_{OH}, was calculated and used as the output for the machine learning model. Through Nørskov's microkinetic model, the reaction site's current density was inferred from ΔG_O - ΔG_{OH} (*22*). The overall avtivity was considered as the sum of the current densities of all CUS in the structure. Gaussian process regression (GPR) was selected for its ability to quantify uncertainty, allowing Bayesian optimization to balance exploration (high-uncertainty regions) and exploitation (high-activity regions) using the expected improvement (EI) acquisition function.

Eight iterations of Bayesian optimization were conducted to identify the most active Ir-TiO_2 configuration (Figures S4-S5). This process generated a dataset of 139 DFT-calculated ΔG_O - ΔG_{OH} values, enabling a machine learning model with a prediction accuracy of 0.06 eV for ΔG_O - ΔG_{OH} (Figure 2A). As shown in Figure 2A, most ΔG_O - ΔG_{OH} values are concentrated in the high-activity region (optimal $\Delta G_O - \Delta G_{OH} \approx 1.53$ eV), confirming that Bayesian optimization effectively prioritizes high-activity regions and avoids the sampling biases typical of random sampling. Separate surrogate models were trained for predicting the adsorption free energy difference ΔG_O - ΔG_{OH} and the thermodynamic stability of the structures. Bayesian optimization was also used to identify the most stable Ir-TiO_2 configuration (Figure S6), resulting in a model with a prediction accuracy of 0.004 eV/atom for formation energy (Figure 2B).

Figure 2C and Figure S7 presents the machine-learning-predicted relative mass activity and relative current density of the most active and most thermodynamic stable structures as a function of Ir loading and Ir surface ratio. The mass activity in this work refers to the Ir mass-specific activity, defined as the catalytic current normalized by the mass of Ir atoms in the system, thereby reflecting the intrinsic utilization efficiency of the precious metal. The relative mass activity and relative current density are both referenced to that of a 4 layer 2×4 rutile IrO_2 model. Even at low doping levels, the addition of Ir significantly boosts mass activity by activating nearby Ti sites, with optimal activity achieved when nearly all CUS Ti sites are engaged. Beyond this optimal Ir ratio, however, further increases in Ir content provide marginal activity enhancement, leading instead to a decay in mass activity due to the excessive Ir loading.

The most active configuration of $IrTiO_2$ at Ir surface ratio of 18% (Figure 2D) displays an ordered arrangement of Ir and Ti atoms, where all Ir atoms are isolated by Ti atoms. This ordered configuration effectively maximizes synergistic interactions between Ir and Ti, resulting in enhanced OER activity due to optimized electronic effects that promote oxygen adsorption and reaction kinetics at Ti sites (Figure S8).

Interestly, the stability Baysian optimization revels a different trend. Configurations with aggregated Ir atoms are thermodynamically more stable (Figure 2E, Figure S6). This trend may be attributed to the collective bonding preferences in different local environments: phase-separated structures feature Ir–O–Ir and Ti–O–Ti linkages, which could be energetically more favorable than the mixed Ir–O–Ti motifs in ordered configurations. In these segregated configurations, fewer Ti sites neighbor Ir atoms, reducing the electron transfer and catalytic synergy necessary for optimal OER performance (Figure S9). As a result, these segregated structures exhibit lower mass activity than the ordered configurations and require a higher Ir surface ratio to achieve optimal mass activity (~50%), as shown in Figure 2C.

The divergence between the most active and most stable configurations outlines the upper and lower bounds of the activity trend under real conditions and highlights the trade-off between maximizing catalytic activity and achieving thermodynamic stability, underscoring the importance of atomic-level design in balancing these properties in Ir-TiO_2 catalysts.

Effects of oxygen vacancy on $IrTiO_2$.

Building on the balance between catalytic activity and thermodynamic stability, we explored strategies to enhance Ti site activation in segregated structures by introducing oxygen vacancies into $IrTiO_2$. To achieve this, a machine learning model was developed to predict OER activity for $IrTiO_{2-x}$, supported by an OER activity database generated by randomly removing oxygen atoms from existing $IrTiO_2$ structures. Approximately 285 DFT-calculated ΔG_O - ΔG_{OH} values for $IrTiO_{2-x}$ were accumulated, with the ΔG_O - ΔG_{OH} distributions for Ti and Ir sites, both with and without oxygen vacancies, shown in Figures 3A and 3B. The introduction of Ir broadens the ΔG_O - ΔG_{OH} distribution for Ti sites, spanning the range between pure TiO_2 and pure IrO_2, while the addition of oxygen vacancies further shifts the ΔG_O - ΔG_{OH} values of Ti toward those of IrO_2. In contrast, the ΔG_O - ΔG_{OH} distribution for Ir sites remains concentrated within a narrow range, indicating that Ir loading and oxygen vacancies have a relatively minor impact on Ir sites.

Using this dataset, we developed a machine learning model for $IrTiO_{2-x}$ with acceptable prediction accuracy of 0.10 eV for ΔG_O - ΔG_{OH} (Figure S10). The model was subsequently employed to optimize oxygen vacancy configurations in $IrTiO_2$ (Figure S11). Figure 3C shows the relative mass activity of the most stable $IrTiO_2$ structures, as well as the maximum activity achieved after introducing a single oxygen vacancy. The results reveal that with 12.5% Ir surface doping and the incorporation of oxygen vacancies, a mass activity exceeding 40 times that of IrO_2 can be achieved. While the surrogate model may not resolve this enhancement with quantitative precision, it effectively captures the qualitative trends and identifies promising configurations for further validation (*23, 24*). To address stability concerns, we additionally calculated the oxygen vacancy formation energies and identified the most stable $IrTiO_{2-x}$ structure (Figure S12), whose predicted mass activity is shown in Figure S13. Despite slightly lower activity compared to the most active $IrTiO_{2-x}$ variant, it still demonstrates a more than 40-fold enhancement over IrO_2, confirming the effectiveness of vacancy engineering in activating Ti sites while retaining structural stability.

To shed light on the activity enhancement mechanism of Ti site by Ir dopant and oxygen vacancy, we analyzed the electronic structure of TiO_2, $IrTiO_2$, $IrTiO_{2-x}$ and IrO_2 through charge density difference and projected density of states (PDOS) calculations. As illustrated in Figure 3D and Figure S14, Ir doping enhances the adsorption affinity of oxygen on Ti site through charge redistribution from Ir to Ti, while the introduction of oxygen vacancies further strengthens the charge transfer. The enhanced charge transfer is quantitatively demonstrated by the Bader charge calculations results, which show that the the charge transfer amounts of the oxygen atom adsorbed on Ti site to the catalyst suface in TiO_2, $IrTiO_2$, and $IrTiO_{2-x}$ are $-0.61|e|$, $-0.67|e|$ and $-0.69|e|$, respectively, and the charge transfer amounts of the iridium atom neighboring to Ti site to the catalyst suface in $IrTiO_2$, and $IrTiO_{2-x}$ are $+1.80|e|$ and $+1.63|e|$. PDOS results reveal that Ir doping introduces new electronic states between the conduction band and valence band of Ti (Figure 3F). Our previous work has shown that Ir doping states raise the highest occupied states (HOS) of the system, which activates otherwise inert Ti sites by increasing energy gain of electrons transferred during O adsorption (*25*). Introducing oxygen vacancies further elevates the HOS, enhancing Ti site activation and improving the conductivity of $IrTiO_2$, which collectively boosts catalytic activity.

Synthesis and characterization of $IrTiO_{2-x}$.

Theoretical predictions suggest that doping with a small amount of Ir and introducing oxygen vacancies can significantly enhance the OER catalytic activity of the IrTi bimetallic oxide material. Following the above theoretical prediction, atomically dispersed Ir on TiO_{2-x} nanorods ($IrTiO_{2-x}$) was synthesized by a simple and scalable impregnation-calcination method. Firstly, TiO_2 nanorod array was grown on carbon cloth (Figure S15) by a hydrothermal method. And then the TiO_{2-x} nanorods with oxygen vacancy was successfully obtained via the calcination of TiO_2 nanorod array at 700 °C for 4 h in H_2/Ar flowing gas, which is confirmed by the EPR signal assigned to oxygen vacancy (Figure S16) (*26, 27*). The X-ray diffraction (XRD) pattern of the TiO_{2-x} nanorods displays a typical rutile structure (JCPD #21-1276) mixed with a small amount of anatase phase (JCPD #21-1272) (Figure S17) (*28*). The scanning electron microscopy (SEM) images show that TiO_{2-x} nanorods have diameters ranging from 50 to 100 nm and a length of around 2 μm (Figure S18). Subsequently, Ir atom was dopped on TiO_{2-x} nanorods by impregnation and calcination process (see Methods for more details), the XRD pattern of $IrTiO_{2-x}$ is consistent with TiO_{2-x} support (Figure S17), and no characteristic diffraction peak related to Ir can be detected, implying the high dispersion of Ir in the catalyst, and the element content of Ir in the catalyst was measured to be 14.2 $\mu g \cdot cm^{-2}$ by inductively coupled plasma optical emission spectroscopy (ICP-OES, Table S5). The morphology of TiO_{2-}

$_x$ nanorods keeps unchanged after the introduce of Ir (Figure S18). High-angle annular dark-field scanning transmission electron microscopy (HAADF-STEM) images of $IrTiO_{2-x}$ present that the well-ordered lattice fringe (0.321 nm) corresponds to the (110) plane of rutile TiO_2, and isolated bright dots (Ir atoms) are randomly scattered on the TiO_{2-x} support (Figure 4A and Figure S19). While our thermodynamic modeling suggests that Ir atoms tend to aggregate in the most stable configurations, this appears to differ from the dispersed Ir distribution observed experimentally. This discrepancy may arise from the kinetic constraints during synthesis, which can lead to metastable states being trapped. EPR spectra of $IrTiO_{2-x}$ further suggests the prominent existence of oxygen vacancy after overgrowth of Ir (Figure 4B).

The chemical state and local coordination environment of Ir species were investigated by X-ray photoelectron spectroscopy (XPS) and X-ray absorption spectroscopy (XAS). Figure S20 shows the XPS spectra of Ir 4f for $IrTiO_{2-x}$ and $IrTiO_2$ catalyst. The binding energy peaks at 62.25 eV and 65.14 eV belong to Ir $4f_{7/2}$ and Ir $4f_{5/2}$, respectively, indicating that the oxidation state of Ir is 4+ (*29, 30*). The X-ray absorption near-edge structure (XANES) spectroscopy of Ir L_3-edge for $IrTiO_{2-x}$ together with Ir foil and IrO_2 as references are presented in Figure 4C. The white line intensity of Ir L_3-edge represents the transition from occupied 2p electron to empty 5d orbital. A more empty Ir 5d orbital state in the catalyst corresponds to the higher intensity of the white line, implying the higher oxidation state of Ir (*31*). Obviously, the white line intensity of $IrTiO_{2-x}$ almost coincides with the commercial IrO_2, demonstrating the valence state of Ir mainly exists in 4+. Moreover, the coordination configurations were analyzed by extended X-ray absorption fine structure (EXAFS). Figure 4D displays the Fourier transform EXAFS spectra of Ir species in the *R*-space. For $IrTiO_{2-x}$, there is no obvious peak at 2.51 Å (for Ir–Ir scattering in metallic Ir), but the dominant peak around 1.63 Å ascribed to the Ir-O bond can be observed, indicating the atomic dispersion of the Ir species in the sample (Figure S21) (*32, 33*).

Electrocatalytic OER performance.

The electrocatalytic performance for OER of $IrTiO_{2-x}$ and TiO_2 was investigated in 0.1 M $HClO_4$ solution at room temperature (experimental details are provided in the Supporting Information). For comparison, the catalytic activities of TiO_2, commercial IrO_2, and 20% Ir/C were also tested under the same conditions. The linear sweep voltammetry (LSV) curves with iR compensation for these catalysts are shown in Figure 4E. Pure TiO_2 exhibits negligible activity, whereas $IrTiO_2$ achieves a lower overpotential (η) of 330 mV to reach a current density of 10 $mA\cdot cm^{-2}$. To enhance the OER activity further, oxygen vacancies were introduced into the catalyst, creating $IrTiO_{2-x}$, which displays high OER activity with an overpotential of only

295 mV at 10 mA·cm^{-2} (Figure 4F), outperforming TiO_2, commercial IrO_2 (410 mV), and 20% Ir/C (382 mV).

Additionally, mass activities were calculated to assess the cost-effectiveness of the atomically dispersed structure. Notably, the mass activity of $IrTiO_{2-x}$ reached 807 A·g_{Ir}^{-1} at 1.53 V (RHE) (Figure 4G, Figure S22), which is 9 times higher than that of commercial IrO_2 (83 A·g_{Ir}^{-1}) and 23 times higher than 20% Ir/C (34 A·g_{Ir}^{-1}). Electrochemically active surface areas (ECSA) were estimated by double-layer capacitance (Cdl) measurements from cyclic voltammetry (CV) with variable scan rates (Figure S23 and Table S6), showing that $IrTiO_{2-x}$ has a higher ECSA than $IrTiO_2$. These results demonstrate the excellent OER activity of $IrTiO_{2-x}$, which can be attributed to the maximized atom efficiency of Ir atoms and the synergistic effect of Ir doping and oxygen vacancies that activate inert Ti sites, validating the theoretical prediction. Furthermore, EPR spectra confirm that the oxygen vacancies in $IrTiO_{2-x}$ remain stable after the OER test (Figure S~~19~~24). Since the EPR spectra were not collected on the same sample before and after OER testing, they cannot conclusively quantify changes in vacancy concentration. Nevertheless, the presence of EPR signals after the OER indicates that oxygen vacancies are retained to a significant extent during the reaction, supporting their structural stability under operating conditions.

In addition, the Tafel slope of $IrTiO_{2-x}$ (68 mV·dec^{-1}) is considerably lower than that of $IrTiO_2$ (79 mV·dec^{-1}), commercial IrO_2 (113 mV·dec^{-1}), and 20% Ir/C (88 mV·dec^{-1}) (Figure 4H), indicating faster OER kinetics for $IrTiO_{2-x}$. The lower charge transfer resistance (Rct) of $IrTiO_{2-x}$, obtained from electrochemical impedance spectroscopy (EIS) analysis, further demonstrates more efficient charge transfer at the $IrTiO_{2-x}$ catalyst-electrolyte interface, implying a faster reaction rate (Figure 4I and Table S7). Furthermore, the performance of $IrTiO_{2-x}$ in terms of mass activity and overpotential surpasses that of most reported Ir-based catalysts for acidic OER (Figure S25 and Table S8). Additionally, the chronopotentiometry measurement was carried out to evaluate the stability of the catalyst. As shown in Figure S26, the overpotential of $IrTiO_{2-x}$ was increased by 60 mV after a continuous operation of more than 10 h at 10 mA cm^{-2}. Compared with the commercial IrO_2 and commercial Ir/C, the $IrTiO_{2-x}$ exhibit a relatively stability.

The *operando* differential electrochemical mass spectrometry (DEMS) experiments with ^{18}O isotope labeling were performed to investigate OER mechanism of $IrTiO_{2-x}$. The different molecular mass involving $^{32}O_2$, $^{34}O_2$ and $^{36}O_2$ during the OER process were collected and analyzed. Firstly, the OER was conducted in 0.1 M $HClO_4$ electrolyte that prepared using ^{18}O-labeled water. As presented in Figure S27a, the reaction predominantly yielded $^{36}O_2$ as the main product, with trace amounts of $^{34}O_2$ detected. This minor $^{34}O_2$ originated from ^{16}O impurities derived from $H_2{}^{16}O$ in the 70% $HClO_4$ electrolyte system or possibly from the lattice oxygen of the catalyst. Subsequently, the second OER test of the catalyst that used in the first step was conducted in 0.1 M $HClO_4$ electrolyte that prepared using ^{16}O-labeled water. As shown in Figure S27b, $^{32}O_2$ was the dominant product, with no detectable $^{34}O_2$ or $^{36}O_2$ signals. This result conflicts with the lattice oxygen-mediated (LOM) mechanism, as the expected exchange of ^{18}O with lattice oxygen in $IrTiO_{2-x}$ during the first OER step would have produced $^{34}O_2$ or $^{36}O_2$ species (*34*). Thus, the DEMS experiments results demonstrated the conventional adsorbate evolution mechanism (AEM), which in agreement with the DFT results. As shown in the LSV curves in Figure S28, we further evaluated the OER catalytic activity of pristine TiO_2 and oxygen-deficient TiO_{2-x}. The results indicate that the introduction of oxygen vacancies leads to negligible changes in catalytic performance, suggesting that oxygen vacancies in TiO_2 do not serve as active sites for the OER. These experimental results confirm that the introduction of oxygen vacancies does not alter the OER mechanism or the active site in for $IrTiO_{2-x}$.

Discussion

In summary, we developed a Bayesian-learning-assisted strategy to design efficient, low-Ir OER catalysts by combining theory and experiment. The resulting Ir-TiO_{2-x} electrocatalyst exhibited significantly improved activity and reduced noble metal usage. Guided by the theory prediction, the successful synthesis and experimental validation of atomically dispersed Ir on TiO_2 nanorods with oxygen vacancies have shown a remarkable enhancement in OER activity. While there are still gaps between theoretical models and specific experimental conditions, they helped narrow the experimental design space by highlighting the importance of balancing Ir content and oxygen vacancy concentration for optimal performance. By leveraging advanced computational techniques and machine learning, this work demonstrates the potential of data-driven catalyst design in advancing renewable energy technologies, aligning with global sustainability goals. The methodologies presented here are not only applicable to OER but could also be extended to other material system, such as suppots like γ-MnO_2 (*14*), and other catalytic reactions like oxygen reduction and carbon dioxide reduction, ultimately contributing to a more sustainable energy future.

Materials and Methods

DFT calculation.

All DFT calculations were performed using the Vienna ab initio simulation package (VASP, version 6.3.2) (*35*). The Perdew-Burke-Ernzerhof (PBE) functional was used to describe the exchange-correlation interactions (*36*). Projector-augmented wave (PAW) method was employed to treat the interaction between the core and valence electrons, the pseudopotentials used treat Ti (3p, 3d, 4s), Ir (5d, 6s), and O (2s, 2p) electrons as valence states. A plane wave basis set with a kinetic energy cutoff of 400 eV was used (*37*). The unit cells of rutile oxides in $P4_2/mnm$ space group were download from Material Project database and reoptimized by DFT. For OER activity calculations for single atom doped oxide, a 2x1 (110) surface model for rutile oxide was constructed with 4-layer-thick slab with 48 atoms. For optimal ratio and configuration calculations for $IrTiO_2$, a larger 4x2 (110) surface model with 4-layer-thick slab with 192 atoms was used. Based on the $IrTiO_2$ model, 1 to 4 oxygen vacancies were randomly removed to model $IrTiO_{2-x}$. Considering that oxygen vacancies on the surface of the bimetallic oxides tend be oxidized and refilled under working conditions, oxygen vacancies were generated in the interior of the slab model rather than on the surface. We also calculated the oxygen vacancy formation energies for both the surface and subsurface layers, and the results show that the formation energy is lower in the subsurface layer than on the surface. Furthermore, oxygen vacancies were not introduced directly at the nearest neighbors of reaction site to avoid creating an overly unsaturated coordination state, which could result in structural reformation during optimization and excessively strong adsorption energies. A vacuum layer of 7.5 Å was added above and below the slab to avoid the periodic interactions. For the slab models, the bottom two atomic layers were fixed during geometry optimization to mimic bulk-like behavior, while the top two layers were fully relaxed. The Monkhorst-Pack k-point mesh for bulk, 2×1 slab and 4×2 slab optimization tasks were 10×10×10, 5×5×1 and 3×3×1, respectively (*38*). In accordance with Vegard's law, the lattice parameters for the $IrTiO_2$ bimetallic oxide model was determined as the weighted average of the lattice parameters of pure TiO_2 and pure IrO_2, based on the stoichiometric ratio of Ti and Ir (*39*) . The optimization was stopped when the energy changes and forces drop below 5×10^{-5} eV and 0.03 eV/Å. DFT+U Hubbard U methods were employed to address the excessive delocalized of d electrons, Hubbard U values were set at 3.3V for Ti element, 3.75V for Mn element and 3.25V for V element. Other U values are adapted from reference (*40*).

The adsorption energies of *O, *OH were calculated by the following Equations:

$$\Delta E_O = E_{O*} - E_* - (E_{H_2O} - E_{H_2}) \quad (1)$$

$$\Delta E_{OH} = E_{OH*} - E_{*} - (E_{H_2O} - 1/2E_{H_2}) \tag{2}$$

where the E_{*}, E_{O*} and E_{OH*} are DFT calculated energies for clean surface, surface with O and OH, respectively. The E_{H_2O} and E_{H_2} are energies of H_2O (-6.76 eV) and H_2 (-14.22 eV) respectively, which are calculated by DFT using a H_2O and H_2 molecule placed on a 10Å×10Å×10Å cubic cell model. The free energy of each adsorbate can be obtained from the following equation:

$$\Delta G = \Delta E + \Delta ZPE - T\Delta S \tag{3}$$

Here the ΔE is the DFT calculated energy, ΔZPE and $T\Delta S$ are the zero point energy correction and entropy correction, respectively. In this work, the $\Delta ZPE - T\Delta S$ values from literature for *OH (0.35 eV), *O (0.05 eV) were used (*15*). The adsorbate evolution mechanism (AEM) consisting of four-step electron-coupled proton transfer steps was used. We also calculated the free energy profile of the LOM pathway on Ir-doped TiO_2 (Figure S29). The results show that the free energy increase of the potential-determining step for LOM is significantly higher than that for AEM, confirming AEM as the more favorable reaction pathway.

The adsorption energies of *O and *OH were computed, and adsorption energies of OOH were obtained using the linear relationship between ΔG_{OOH} and ΔG_{OH}($\Delta G_{OOH} = \Delta G_{OH} + 3.2$ eV) (*15*). The reaction free energies of four OER elementary step can be obtained by:

$$\Delta G_1 = \Delta G_{OH} \tag{4}$$

$$\Delta G_2 = \Delta G_O - \Delta G_{OH} \tag{5}$$

$$\Delta G_3 = \Delta G_{OOH} - \Delta G_O \tag{6}$$

$$\Delta G_4 = 4.92 - \Delta G_{OOH} \tag{7}$$

The overpotential is calculated by the following equation:

$$\eta = \max(\Delta G_i)/e - 1.23V \tag{8}$$

Here $\max(\Delta G_i)$ is the maximum reaction free energy of four elementary steps.

A microkinetic modeling correlating the $\Delta G_O - \Delta G_{OH}$ with current density was applied to evaluate the OER activity of each reaction site at an applied potential of 1.53 V (*41*). The logarithm of the current density (log i) was approximated as a piecewise linear function as following:

$$\log i = \begin{cases} 8.06 \times \Delta G - 12.98, \Delta G < 1.53\text{eV} \\ -8.74 \times \Delta G + 12.73, \Delta G \geq 1.53\text{eV} \end{cases} \tag{9}$$

Where ΔG is the free energy difference of the reaction from *OH to *O. The activity of a given configuration was evaluated as the average current density over all its CUS sites. The theoretical relative mass activity was computed by dividing the mass activity of $IrTiO_2$ by that of IrO_2 using a 4-layer slab model. The formation energy was used to reflect the thermodynamic stability, which is defined by the following equation:

$$E_f = E(Ir_xTi_{1-x}O_2) - [xE(IrO_2) + (1-x)E(TiO_2)] \qquad (10)$$

Where E(*) is the DFT calculated energy of $Ir_xTi_{1-x}O_2$ model, x is the stoichiometric surface ratio of Ir in $Ir_xTi_{1-x}O_2$, $E(TiO_2)$ and $E(IrO_2)$ depict the DFT calculated energies when the surface ratio of Ir are 0 and 1, respectively.

Feature Engineering

To develop a machine learning model capable of predicting intermediate adsorption energies on oxide coordinately unsaturated site, we digitally encode the atomic neighboring environment of CUS as input for the machine learning model, as depicted in Figure S3. The metal atoms closest to the CUS site in the oxide were divided into four atomic layers. Starting from the nearest to the farthest layer from the CUS, there are 1, 2, 2, 4 and 2 atoms in each of the five layers, respectively. To enhance the fidelity of feature, the second neighboring layer is subdivided into its own second and fourth neighboring layers, and the fourth neighboring layer is also subdivided into its own second and fourth neighboring layers. Consequently, the neighboring environment of the adsorption site is subdivided into nine atomic layers. The number of Ti atoms, number of Ir atoms, mean coordination number of Ti atoms, mean coordination number of Ir atoms were used to quantify all nine atomic layers, which made up the 36-dimensional feature. When there are two Ir atoms and two Ti atoms in the fourth neighbor atomic shell of the CUS site, there are three different environments resulting from the atomic occupations. We included angles as part of the features to describe these environments. Additionally, we utilized the overall Ir doping ratio in alloy oxide as an additional dimensional feature. When introducing oxygen vacancies, the oxygen vacancies reduce the coordination number of metal atoms, which is subsequently reflected in the feature. Normalization was employed to eliminate bases caused by varying feature values across different dimensions. Principal Component Analysis (PCA) dimensionality reduction was utilized to delete redundant features. The DFT calculated $\Delta G_O - \Delta G_{OH}$ values of CUS site were used as the output for the ML model.

Machine learning model capable of predicting stability for given doped $IrTiO_2$ configuration was also developed. The features for the model were extracted by counting the numbers of different coordination pairs in for 5-coordinated CUS 6-coordinated bridge site. The DFT calculated energy of $IrTiO_2$ with the reference energies of pure TiO_2 and IrO_2 phases was used as the output target.

Machine learning and Bayesian optimization

We choose the Gaussian Process Regression (GPR) model for its capacity to estimate uncertainties. The radial-basis function (RBF) was used to determine the term in covariance matrix. The RBF function was defined as:

$$k(x,x') = a^2\exp(-\frac{(x-x')^2}{2b^2}) \qquad (11)$$

Where x and x' were two variables, a and b were scale factor and length factor, and these two factors were optimized in machine learning model training. The scikit-learn package was used for constructing GPR model (*42*). The predicted $\Delta G_O - \Delta G_{OH}$ and corresponding uncertainty of each CUS site in $IrTiO_2$ model were further translated to OER activity A and corresponding uncertainty σ_A. The hypothesis is put forward that the OER activity A of each site behaves as an independent random variable drawn from a population that follows a normal distribution $N(A, \sigma_A^2)$. Then the mean activity $\overline{A}$ of all 8 CUS site in $IrTiO_2$ model can be regarded as a random variable satisfying Gaussian distribution in the following form:

$$\overline{A} = N(\sum_{i=1}^{8} A_i, 1/8\sum_{i=1}^{8} \sigma_{A_i}^2) \qquad (12)$$

The expected improvement (EI) was used as the acquisition function to determine the selection of the next $IrTiO_2$ configuration. EI is defined as followed:

$$EI(x) = [f(x) - f(x^+) - \zeta]\Phi(Z) + \sigma(x)\phi(Z) \qquad (13)$$

Where $Z = [f(x) - f(x^+)]/\sigma(x)$, $f(x^+)$ is the maximum value in existing dataset, Φ and ϕ are the cumulative density and probability density function of standard normal distribution, respectively. ζ is a hyperparameter in EI function, in this work a constant value 0.01 was used for ζ. $f(x)$ and $\sigma(x)$ are the predicted mean activity and uncertainty for a given $IrTiO_2$ structure as described in Equation (12).

Since binary oxide structures are intractable to be completely enumerate, we conducted Monte Carlo simulation to find the configurations with the highest EI values at various Ir ratio and oxygen vacancy locations. Totally 8 oxide structures were chosen in each iteration (7 structures with equal-ratio from 12.5% to 87.5%, and 1 structure with the highest EI), the $\Delta G_O -$

ΔG_{OH} of these searched structures were calculated by DFT calculation and added to the training database to refine the machine learning surrogate model.

Materials.

Tetrabutyl orthotitanate (≥99%) and isopropanol were purchased from Aladdin. Chloroiridic acid (H_2IrCl_6, 35% Ir) was purchased from Macklin. Perchloric acid ($HClO_4$, 70%) was purchased from Sigma-Aldrich. Ethanol and hydrochloric acid (HCl) were purchased from Beijing Tong Guang fine chemical company. Commercial IrO_2 was purchased from Henan Bauhinia Chemical Technology Co., Ltd. Carbon cloth (WOS 1011) was purchased from Taiwan CeTech Co., Ltd and further treated with nitric acid (HNO_3). Carbon paper (TGP-H-060) was purchased from TORAY.

Synthesis of TiO_2 nanorod array. The TiO_2 nanorod array supported on carbon cloth was firstly prepared by a seed-assisted hydrothermal process (*28*). Typically, a piece of carbon cloth (1×1 cm^2) was soaked in isopropanol containing 75 mM titanium butoxide for 3 min. The precursor was dried at 60 °C and then annealed at 400 °C with heating rate of 2 °C/min for 2 h in air to form a thin layer of TiO_2 seeds. The carbon cloth with TiO_2 seeds was transferred in Teflon-lined stainless-steel autoclave and immersed in a solution containing 5 mL 6 M HCl and 100 μL titanium butoxide. Subsequently, the autoclave was heated at 150 °C for 8 h. After that, the hydrothermally treated carbon cloth was calcined at 400 °C with heating rate of 10 °C/min for 2 h in air.

Synthesis of TiO_{2-x} nanorod array. The TiO_2 nanorod array was annealed at 700 °C for 4 h in H_2/Ar flowing gas to prepare the defective TiO_2 (named as TiO_{2-x}) nanorod array. Although surface vacancies are preferentially generated during H_2 treatment, their instability under oxidative conditions suggests that only subsurface or near-surface vacancies remain active during OER. This supports the relevance of our computational model, which emphasizes the role of stable subsurface oxygen vacancies in enhancing catalytic activity.

Synthesis of Ir single atoms on TiO_{2-x} nanorod ($IrTiO_{2-x}$). The $IrTiO_{2-x}$ catalyst was synthesized by an impregnation-thermal decomposition process. In detail, the piece of carbon cloth loaded with TiO_{2-x} nanorod array was immersed in 0.5 mg/mL H_2IrCl_6 solution for 4 h. the $IrTiO_{2-x}$ was obtained by calcining the precursor sample at 300 °C with heating rate of 5 °C/min for 2 h under argon atmosphere.

Synthesis of Ir single atoms on TiO_2 nanorod ($IrTiO_2$). The $IrTiO_2$ catalyst was prepared by the same method with $IrTiO_{2-x}$, except that using TiO_2 nanorod array instead of TiO_{2-x}.

Characterizations.

Field emission scanning electron m icroscope (FE-SEM) was collected on a HITACHI SU-8010 microscope. High-resolution transmission electron microscopy (HRTEM) was performed on a JEOL JEM-2100F microscope operated at 200 kV. High-angle annular dark field-scanning transmission electron microscopy (HADDF-STEM) images of the catalysts were obtained on Thermo Scientific Themis Z microscope working at 300 kV. Powder X-ray diffraction (XRD) patterns were performed on a PANalytical X'Pert PRO diffractometer with Cu-Kα radiation (λ=1.5418 Å, 40 kV, 40 mA). X-ray photoelectron spectroscopy (XPS) was collected on Thermo Scientific K-Alpha, and all data were corrected with C 1s peak at 284.6 eV. Inductively coupled plasma optical emission spectroscopy (ICP-OES) was carried out by using Agilent 5110. Electron paramagnetic resonance (EPR) measurements were run on a Bruker EMX PLUS spectrometer. The X-ray absorption spectroscopy (XAS) data were collected at the 1W1B station in Beijing Synchrotron Radiation Facility (BSRF), the X-ray absorption nearedge spectroscopy (XANES) and at Ir L_3-edge of catalysts were obtained with fluorescence mode. The XAS data at Ir L_3-edge were calibrated to Ir foil, and IrO_2 was used as reference materials. The data analysis was performed using Artemis and Athena in the Demeter software suite by FEFF software.

Electrochemical measurements.

The OER performance of the catalysts was studied on a CHI 760E workstation with a standard three-electrode cell. The carbon cloth substrate supported with $IrTiO_{2-x}$ nanorod array was used as a working electrode. An Ag/AgCl electrode (saturated KCl) and platinum plate (1 × 1 cm) were served as the reference electrode and counter electrode, respectively. All measurements were performed in 0.1 M $HClO_4$ electrolyte at room temperature. All potentials in this work were converted into the reversible hydrogen electrode (RHE) by the equation of E (*vs*. RHE) = E (*vs*. Ag/AgCl) + 0.27 V.

The linear sweep voltammetry (LSV) was recorded in the potential range of 1–2 V *vs.* RHE with a scan rate of 5 $mV\cdot s^{-1}$ after being calibrated with iR compensation. The electrochemical impedance spectroscopy (EIS) was conducted at an overpotential of 0.3 V from 0.1 to 10^5 Hz. The load amount of commercial IrO_2 and 20% Ir/C on the carbon paper are 30 $\mu g_{Ir}.cm^{-2}$ and 15 $\mu g_{Ir}.cm^{-2}$. The mass activity (MA) of catalysts was obtained by the equation of j_{geo}/m_{Ir}, where

j_{geo} is the geometric current density (mA·cm^{-2}), m_{Ir} is the loading of Ir on the carbon cloth (μg$_{\mathrm{Ir}}$·cm^{-2}), which is obtained from ICP-OES results. The electrochemically active surface area (ECSA) was estimated by electrochemical double-layer capacitance (C_{dl}) according to the equation of C_{dl}/C_s, where C_{dl} was tested in the non-Faradic potential of 1.1–1.2 V *vs.* RHE with a scan rate from 10 to 50 mV·s^{-1}. The C_s is the specific capacitance and the value is chosen as 35 μF·cm^{-2} to estimate the ECSA.

Data and Materials Availability

All other data needed to evaluate the conclusions in this paper are present in the paper and/or the Supplementary Materials. Additional datasets and trained machine learning models are available at Zenodo database: https://zenodo.org/records/15477808.

References

1. H. Xie, Z. Zhao, T. Liu, Y. Wu, C. Lan, W. Jiang, L. Zhu, Y. Wang, D. Yang, Z. Shao, A membrane-based seawater electrolyser for hydrogen generation. *Nature* **612**, 673-678 (2022).
2. H. Nishiyama, T. Yamada, M. Nakabayashi, Y. Maehara, M. Yamaguchi, Y. Kuromiya, Y. Nagatsuma, H. Tokudome, S. Akiyama, T. Watanabe, R. Narushima, S. Okunaka, N. Shibata, T. Takata, T. Hisatomi, K. Domen, Photocatalytic solar hydrogen production from water on a 100-m2 scale. *Nature* **598**, 304-307 (2021).
3. H. B. Tao, H. Liu, K. Lao, Y. Pan, Y. Tao, L. Wen, N. Zheng, The gap between academic research on proton exchange membrane water electrolysers and industrial demands. *Nature Nanotechnology* **19**, 1074-1076 (2024).
4. R.-T. Liu, Z.-L. Xu, F.-M. Li, F.-Y. Chen, J.-Y. Yu, Y. Yan, Y. Chen, B. Y. Xia, Recent advances in proton exchange membrane water electrolysis. *Chemical Society Reviews* **52**, 5652-5683 (2023).
5. H.-S. Oh, H. N. Nong, T. Reier, A. Bergmann, M. Gliech, J. Ferreira de Araújo, E. Willinger, R. Schlögl, D. Teschner, P. Strasser, Electrochemical catalyst–support effects and their stabilizing role for IrO x nanoparticle catalysts during the oxygen evolution reaction. *Journal of the American Chemical Society* **138**, 12552-12563 (2016).
6. X. Liang, L. Shi, Y. Liu, H. Chen, R. Si, W. Yan, Q. Zhang, G. D. Li, L. Yang, X. Zou, Activating inert, nonprecious perovskites with iridium dopants for efficient oxygen evolution reaction under acidic conditions. *Angewandte Chemie International Edition* **58**, 7631-7635 (2019).
7. A. Akbashev, L. Zhang, J. Mefford, J. Park, B. Butz, H. Luftman, W. Chueh, A. Vojvodic, Activation of ultrathin SrTiO3 with subsurface SrRuO 3 for the oxygen evolution reaction. *Energy & Environmental Science* **11**, 1762-1769 (2018).
8. Z. Pei, H. Zhang, Z.-P. Wu, X. F. Lu, D. Luan, X. W. Lou, Atomically dispersed Ni activates adjacent Ce sites for enhanced electrocatalytic oxygen evolution activity. *Science Advances* **9**, eadh1320 (2023).
9. L. Xu, Q. Jiang, Z. Xiao, X. Li, J. Huo, S. Wang, L. Dai, Plasma‐engraved Co3O4 nanosheets with oxygen vacancies and high surface area for the oxygen evolution reaction. *Angewandte Chemie* **128**, 5363-5367 (2016).

10. L. Zhuang, L. Ge, Y. Yang, M. Li, Y. Jia, X. Yao, Z. Zhu, Ultrathin iron ‐ cobalt oxide nanosheets with abundant oxygen vacancies for the oxygen evolution reaction. *Advanced Materials* **29**, 1606793 (2017).
11. J. Shan, Y. Zheng, B. Shi, K. Davey, S.-Z. Qiao, Regulating electrocatalysts via surface and interface engineering for acidic water electrooxidation. *ACS Energy Letters* **4**, 2719-2730 (2019).
12. X. Wang, Y. Huang, X. Xie, Y. Liu, Z. Huo, M. Lin, H. Xin, R. Tong, Bayesian-optimization-assisted discovery of stereoselective aluminum complexes for ring-opening polymerization of racemic lactide. *Nature Communications* **14**, 3647 (2023).
13. T. Mou, H. S. Pillai, S. Wang, M. Wan, X. Han, N. M. Schweitzer, F. Che, H. Xin, Bridging the complexity gap in computational heterogeneous catalysis with machine learning. *Nature Catalysis* **6**, 122-136 (2023).
14. A. Li, S. Kong, K. Adachi, H. Ooka, K. Fushimi, Q. Jiang, H. Ofuchi, S. Hamamoto, M. Oura, K. Higashi, Atomically dispersed hexavalent iridium oxide from MnO2 reduction for oxygen evolution catalysis. *Science* **384**, 666-670 (2024).
15. I. C. Man, H. Y. Su, F. Calle ‐ Vallejo, H. A. Hansen, J. I. Martínez, N. G. Inoglu, J. Kitchin, T. F. Jaramillo, J. K. Nørskov, J. J. C. Rossmeisl, Universality in oxygen evolution electrocatalysis on oxide surfaces. *ChemCatChem* **3**, 1159-1165 (2011).
16. J. Rossmeisl, Z. W. Qu, H. Zhu, G. J. Kroes, J. K. Nørskov, Electrolysis of water on oxide surfaces. *Journal of Electroanalytical Chemistry* **607**, 83-89 (2007).
17. W. Zhu, X. Song, F. Liao, H. Huang, Q. Shao, K. Feng, Y. Zhou, M. Ma, J. Wu, H. Yang, H. Yang, M. Wang, J. Shi, J. Zhong, T. Cheng, M. Shao, Y. Liu, Z. Kang, Stable and oxidative charged Ru enhance the acidic oxygen evolution reaction activity in two-dimensional ruthenium-iridium oxide. *Nature Communications* **14**, 5365 (2023).
18. S. Divanis, A. M. Frandsen, T. Kutlusoy, J. Rossmeisl, Lifting the discrepancy between experimental results and the theoretical predictions for the catalytic activity of RuO 2 (110) towards oxygen evolution reaction. *Physical Chemistry Chemical Physics* **23**, 19141-19145 (2021).
19. M. García ‐ Mota, A. Vojvodic, H. Metiu, I. C. Man, H. Y. Su, J. Rossmeisl, J. K. Nørskov, Tailoring the activity for oxygen evolution Electrocatalysis on rutile TiO2 (110) by transition ‐ metal substitution. *ChemCatChem* **3**, 1607-1611 (2011).
20. H. P. Tran, H. N. Nong, M. Zlatar, A. Yoon, U. Hejral, M. Rüscher, J. Timoshenko, S. r. Selve, D. Berger, M. Kroschel, Reactivity and Stability of Reduced Ir-Weight TiO2-Supported Oxygen Evolution Catalysts for Proton Exchange Membrane (PEM) Water Electrolyzer Anodes. *Journal of the American Chemical Society* **146**, 31444-31455 (2024).
21. J. Park, E. Liu, S. Angizi, A. Abdellah, E. Y. Kirici, D. Higgins, Formation of Core ‐ Shell Ir@ TiO2 Nanoparticles through Hydrogen Treatment as Acidic Oxygen Evolution Reaction Catalysts. *Advanced Functional Materials* **34**, 2408848 (2024).
22. I. C. Man, H.-Y. Su, F. Calle-Vallejo, H. A. Hansen, J. I. Martínez, N. G. Inoglu, J. Kitchin, T. F. Jaramillo, J. K. Nørskov, J. Rossmeisl, Universality in Oxygen Evolution Electrocatalysis on Oxide Surfaces. *ChemCatChem* **3**, 1159-1165 (2011).
23. S. Back, K. Tran, Z. W. Ulissi, Toward a design of active oxygen evolution catalysts: insights from automated density functional theory calculations and machine learning. *ACS Catalysis* **9**, 7651-7659 (2019).
24. J. Zhang, C. Wang, S. Huang, X. Xiang, Y. Xiong, B. Xu, S. Ma, H. Fu, J. Kai, X. Kang, Design high-entropy electrocatalyst via interpretable deep graph attention learning. *Joule* **7**, 1832-1851 (2023).
25. L. Zhang, A. S. Raman, A. Vojvodic, Reviving Inert Oxides for Electrochemical Water Splitting by Subsurface Engineering. *Chemistry of Materials* **32**, 5569-5578 (2020).

26. X. Wang, X. Wan, X. Qin, C. Chen, X. Qian, Y. Guo, Q. Xu, W.-B. Cai, H. Yang, K. Jiang, Electronic Structure Modulation of RuO2 by TiO2 Enriched with Oxygen Vacancies to Boost Acidic O2 Evolution. *ACS Catalysis* **12**, 9437-9445 (2022).
27. J. Wang, W. Lin, Y. Ran, J. Cui, L. Wang, X. Yu, Y. Zhang, Nanotubular TiO2 with Remedied Defects for Photocatalytic Nitrogen Fixation. *The Journal of Physical Chemistry C* **124**, 1253-1259 (2019).
28. Z. Gu, Z. Zhang, N. Ni, C. Hu, J. Qu, Simultaneous phenol removal and resource recovery from phenolic wastewater by electrocatalytic hydrogenation. *Environmental Science & Technology* **56**, 4356-4366 (2022).
29. Q. Wang, X. Huang, Z. L. Zhao, M. Wang, B. Xiang, J. Li, Z. Feng, H. Xu, M. Gu, Ultrahigh-loading of Ir single atoms on NiO matrix to dramatically enhance oxygen evolution reaction. *Journal of the American Chemical Society* **142**, 7425-7433 (2020).
30. Z. Xu, L. Zhou, G. Zhou, S. Wu, P. Wang, H. Li, P. Huang, L. Liu, Light‐driven orderly assembly of Ir‐atomic chains to integrate a dynamic reaction pathway for acidic oxygen evolution. *Angewandte Chemie* **135**, e202301128 (2023).
31. Z. Shi, Y. Wang, J. Li, X. Wang, Y. Wang, Y. Li, W. Xu, Z. Jiang, C. Liu, W. Xing, J. Ge, Confined Ir single sites with triggered lattice oxygen redox: Toward boosted and sustained water oxidation catalysis. *Joule* **5**, 2164-2176 (2021).
32. Y. Lu, T. Liu, C. L. Dong, Y. C. Huang, Y. Li, J. Chen, Y. Zou, S. Wang, Tuning the selective adsorption site of biomass on Co3O4 by Ir single atoms for electrosynthesis. *Advanced Materials* **33**, 2007056 (2021).
33. F. Luo, H. Hu, X. Zhao, Z. Yang, Q. Zhang, J. Xu, T. Kaneko, Y. Yoshida, C. Zhu, W. Cai, Robust and stable acidic overall water splitting on Ir single atoms. *Nano Letters* **20**, 2120-2128 (2020).
34. J. Xu, H. Jin, T. Lu, J. Li, Y. Liu, K. Davey, Y. Zheng, S.-Z. Qiao, IrO x· n H2O with lattice water–assisted oxygen exchange for high-performance proton exchange membrane water electrolyzers. *Science Advances* **9**, eadh1718 (2023).
35. G. Kresse, J. Furthmüller, Efficient iterative schemes for ab initio total-energy calculations using a plane-wave basis set. *Physical Review B* **54**, 11169-11186 (1996).
36. J. P. Perdew, K. Burke, M. Ernzerhof, Generalized gradient approximation made simple. *Physical Review Letters* **77**, 3865 (1996).
37. G. Kresse, D. Joubert, From ultrasoft pseudopotentials to the projector augmented-wave method. *Physical Review B* **59**, 1758 (1999).
38. H. J. Monkhorst, J. D. Pack, Special points for Brillouin-zone integrations. *Physical Review B* **13**, 5188-5192 (1976).
39. N. Ashcroft, A. Denton, Vegard's law. *Physical Review A* **43**, 3161-3164 (1991).
40. B. M. Comer, J. Li, F. Abild-Pedersen, M. Bajdich, K. T. Winther, Unraveling Electronic Trends in O* and OH* Surface Adsorption in the MO2 Transition-Metal Oxide Series. *The Journal of Physical Chemistry C* **126**, 7903-7909 (2022).
41. C. F. Dickens, C. Kirk, J. K. Nørskov, Insights into the Electrochemical Oxygen Evolution Reaction with ab Initio Calculations and Microkinetic Modeling: Beyond the Limiting Potential Volcano. *The Journal of Physical Chemistry C* **123**, 18960-18977 (2019).
42. F. Pedregosa, G. Varoquaux, A. Gramfort, V. Michel, B. Thirion, O. Grisel, M. Blondel, P. Prettenhofer, R. Weiss, V. Dubourg, Scikit-learn: Machine learning in Python. *The Journal of Machine Learning Research* **12**, 2825-2830 (2011).

Acknowledgements

This work was sponsored by Tsinghua University-Toyota Joint Research Center for Hydrogen Energy and Fuel Cell Technology of Vehicles.

Author contributions

Conceptualization: LZ
Methodology: XFN, YJC
Investigation: XFN, YJC, MZS
Visualization: XFN, YJC
Resources: LZ, ZQN, SN, YA
Supervision: LZ, ZQN
Writing—original draft: XFN, YJC
Writing—review & editing: XFN, YJC, LZ, ZQN

Competing interests: X.N., Z.L., S.N., Y.A., Y.C. and Z.N. filed a provisional patent application (patent application number: 2024112232821). S.N. and Y.A. are employees of Toyota Motor Corporation. The authors declare no other competing interests.

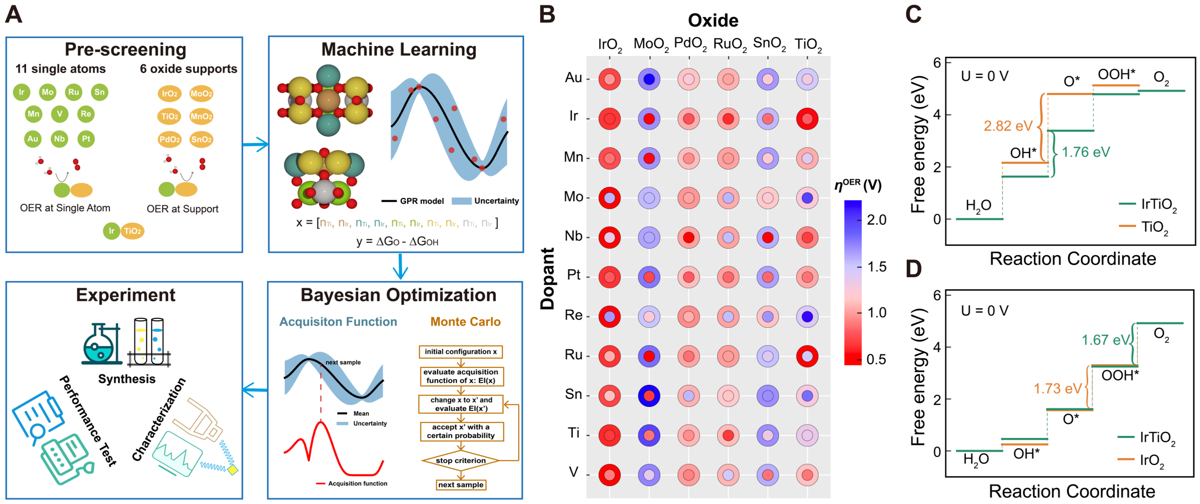

Fig. 1 | Workflow and bimetallic oxide combination screening. (A) Workflow of the Bayesian optimization accelerating the design of OER electrocatalyst. **(B)** DFT calculated heatmap of oxygen evolution reaction activity for various dopant-support combinations. The OER overpotential is represented by the color-coding double ring, with red indicating low overpotential and blue indicating high overpotential. The inner circles denote the overpotential when dopant atoms act as reaction sites, while the outer rings indicate the overpotential for metal sites in the oxide serving as reaction sites. **(C)** Free energy profiles of oxygen evolution reaction on Ti site in pure TiO_2 (orange) and Ir doped TiO_2 (green). **(D)** Free energy profiles of oxygen evolution reaction on Ir site in pure IrO_2 (orange) and Ir doped TiO_2 (green).

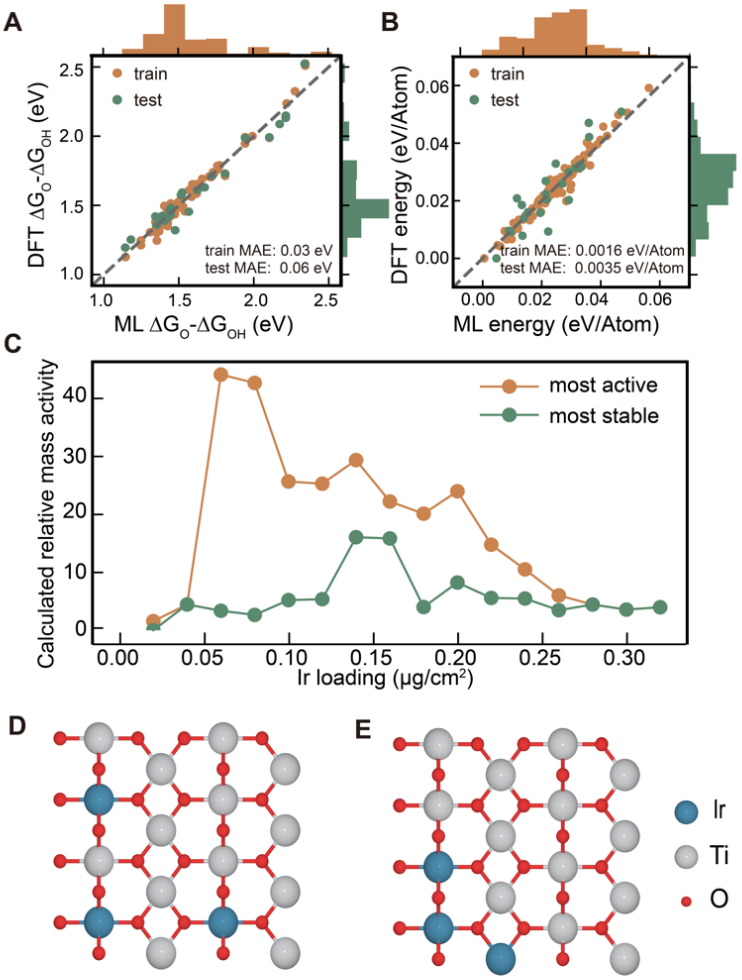

Fig. 2 | Bayesian optimization of IrTiO$_2$. **(A)** Parity plot of the machine learning model predicting $\Delta G_O - \Delta G_{OH}$ for IrTiO$_2$. **(B)** Parity plot of the machine learning model predicting formation energy for IrTiO$_2$. The reported mean absolute error of the surrogate model (in eV/atom) is normalized to the total number of atoms in the slab, including all elements. The train-to-test set ratio is 8:2, and the reported mean absolute error (MAE) is the average of 10 random cross-validation runs. **(C)** Machine learning predicted mass activity (relative to IrO$_2$) at 1.53V as a function of Ir loading for the most active and the most stable IrTiO$_2$ configuration. **(D)** The most active IrTiO$_2$ oxide configuration at Ir surface ratio of 18.75%. **(E)** The most stable IrTiO$_2$ oxide configuration at Ir surface ratio of 18.75%.

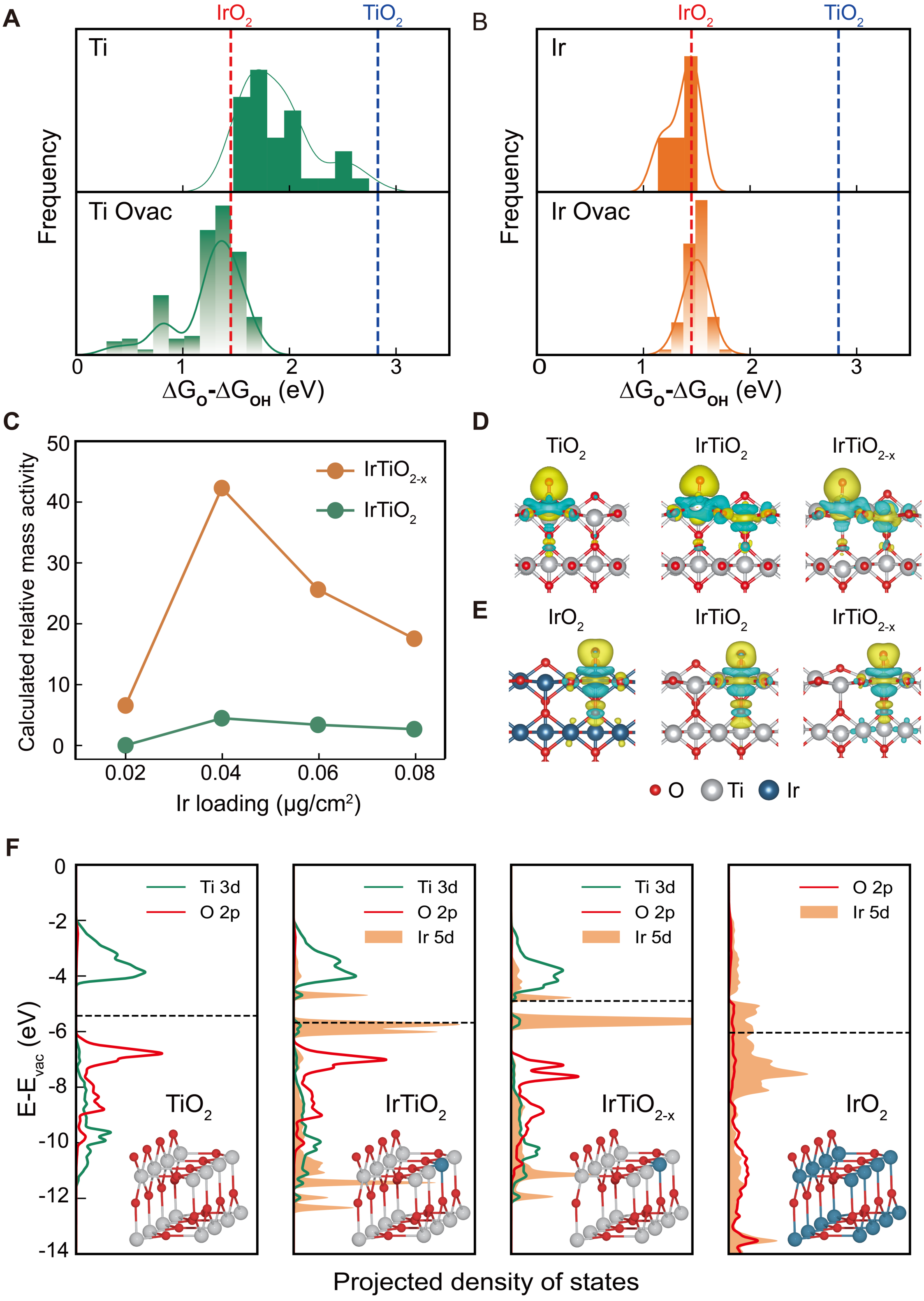

Fig. 3 | Effect of oxygen vacancies on the OER activity of IrTiO$_2$. (A) Frequency distribution histogram of $\Delta G_O - \Delta G_{OH}$ on Ti sites without and with oxygen vacancies. **(B)** Frequency distribution histogram of $\Delta G_O - \Delta G_{OH}$ on Ir sites without and with oxygen vacancies. The vertical dashed lines in blue and red respectively depict the $\Delta G_O - \Delta G_{OH}$ values of pure TiO_2 and pure IrO_2. **(C)** Machine learning predicted mass activity at 1.53V relative to IrO_2 of $IrTiO_2$ and $IrTiO_{2-x}$ as a function of Ir loading. **(D)** Charge density differences calculations of O adsorbed on Ti site in pure TiO_2, $IrTiO_2$ and $IrTiO_{2-x}$, yellow signifies charge accumulation and cyan indicates charge depletion. **(E)** Charge density differences calculations of O adsorbed on Ir site in pure IrO_2, $IrTiO_2$ and $IrTiO_{2-x}$ **(F)** DFT calculated projected density of states (PDOS) of TiO_2, $IrTiO_2$, and $IrTiO_{2-x}$ and IrO_2. The 2p states of O atoms, 3d states of Ti atoms and 5d states of Ir atoms in the surface are colored by red, green and orange, respectively. The energies are all referenced to the vacuum level, and the Fermi level for each system was denoted by the vertical black dashed line.

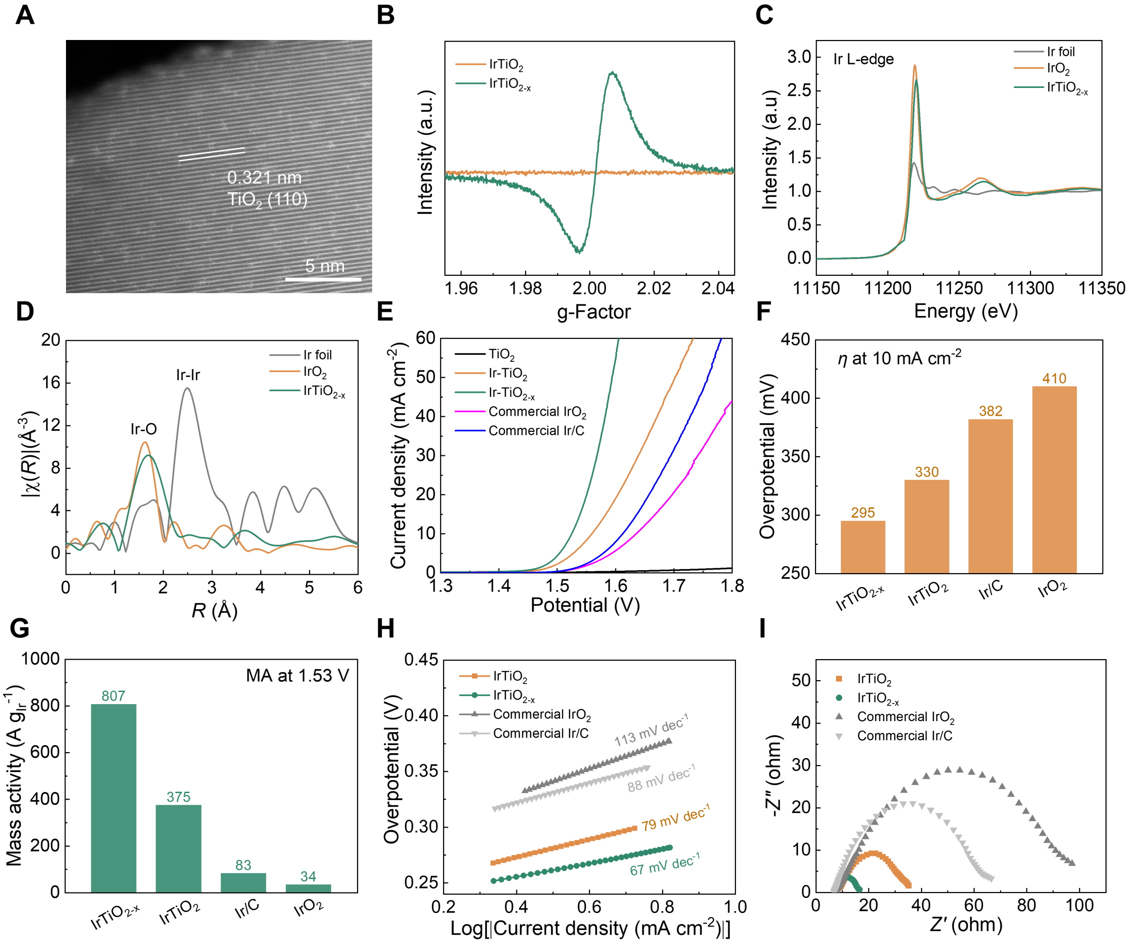

Fig. 4 | Characterization and electrocatalytic OER performance of catalysts. (**A**) HAADF-STEM images of $IrTiO_{2-x}$. (**B**) EPR spectra of $IrTiO_2$ and $IrTiO_{2-x}$. (**C**) Ir L_3-edge XANES spectra of $IrTiO_{2-x}$, commercial IrO_2, and Ir foil. (**D**) Fourier-transforms of k^3-weight Ir L_3-edge EXAFS spectra for $IrTiO_{2-x}$, commercial IrO_2, and Ir foil. (**E**) LSV curves of TiO_2, $IrTiO_2$, $IrTiO_{2-x}$, commercial IrO_2 and 20% Ir/C. (**F**) Overpotential of $IrTiO_2$, and $IrTiO_{2-x}$, commercial IrO_2, and 20% Ir/C at 10 $mA{\cdot}cm^{-2}$. (**G**) Mass activity of $IrTiO_2$, and $IrTiO_{2-x}$, commercial IrO_2, and 20% Ir/C at 1.53 V vs. RHE. (**H**) Tafel slopes derived from (E). (**I**) EIS plots of $IrTiO_2$, and $IrTiO_{2-x}$, commercial IrO_2, and 20% Ir/C.